scientific reports

OPEN

An insight into thermal properties of BC$_3$-graphene hetero-nanosheets: a molecular dynamics study

Maryam Zarghami Dehaghani[1], Fatemeh Molaei[2], Farrokh Yousefi[3], S. Mohammad Sajadi[4,5], Amin Esmaeili[6], Ahmad Mohaddespour[7], Omid Farzadian[8], Sajjad Habibzadeh[9 ✉], Amin Hamed Mashhadzadeh[8 ✉], Christos Spitas[8] & Mohammad Reza Saeb[10]

Simulation of thermal properties of graphene hetero-nanosheets is a key step in understanding their performance in nano-electronics where thermal loads and shocks are highly likely. Herein we combine graphene and boron-carbide nanosheets (BC3N) heterogeneous structures to obtain BC3N-graphene hetero-nanosheet (BC3GrHs) as a model semiconductor with tunable properties. Poor thermal properties of such heterostructures would curb their long-term practice. BC$_3$GrHs may be imperfect with grain boundaries comprising non-hexagonal rings, heptagons, and pentagons as topological defects. Therefore, a realistic picture of the thermal properties of BC$_3$GrHs necessitates consideration of grain boundaries of heptagon-pentagon defect pairs. Herein thermal properties of BC$_3$GrHs with various defects were evaluated applying molecular dynamic (MD) simulation. First, temperature profiles along BC$_3$GrHs interface with symmetric and asymmetric pentagon-heptagon pairs at 300 K, ΔT = 40 K, and zero strain were compared. Next, the effect of temperature, strain, and temperature gradient (ΔT) on Kaptiza resistance (interfacial thermal resistance at the grain boundary) was visualized. It was found that Kapitza resistance increases upon an increase of defect density in the grain boundary. Besides, among symmetric grain boundaries, 5–7–6–6 and 5–7–5–7 defect pairs showed the lowest (2×10^{-10} m^2 K W^{-1}) and highest (4.9×10^{-10} m^2 K W^{-1}) values of Kapitza resistance, respectively. Regarding parameters affecting Kapitza resistance, increased temperature and strain caused the rise and drop in Kaptiza thermal resistance, respectively. However, lengthier nanosheets had lower Kapitza thermal resistance. Moreover, changes in temperature gradient had a negligible effect on the Kapitza resistance.

Graphene, sp^2-hybridized carbon, with honeycomb crystal lattice, has received considerable attention from its first production due to possessing outstanding features such as superior Young's modulus (1000–1500 GPa)[1], high adsorption capacity[2], excellent thermal conductivity (5000 W m^{-1} K^{-1})[3–5], desirable electrical conductivity (2000s m^{-1})[6], and large surface area (2630 m^2 g^{-1})[7]. Therefore, graphene supports various fields such as biological, environmental, and engineering applications[8–13]. On the other hand, graphene suffers from zero bandgap, limiting its usefulness as a semiconductor or transistor. Therefore, the inevitable hybridization of graphene with non-zero bandgap nanosheets such as boron-nitride (BN)[14–19], boron-carbide (BC$_3$)[20,21], nitrogen-carbide (C$_3$N)[22],

[1]Center of Excellence in Electrochemistry, School of Chemistry, College of Science, University of Tehran, Tehran, Iran. [2]Mining and Geological Engineering Department, The University of Arizona, Arizona, USA. [3]Department of Physics, University of Zanjan, 45195-313 Zanjan, Iran. [4]Department of Nutrition, Cihan University-Erbil, Kurdistan Region, Erbil, Iraq. [5]Department of Phytochemistry, SRC, Soran University, KRG, Erbil, Iraq. [6]Department of Chemical Engineering, College of the North Atlantic—Qatar, 24449 Arab League St, PO Box 24449, Doha, Qatar. [7]College of Engineering and Technology, American University of the Middle East, Egaila, Kuwait. [8]Mechanical and Aerospace Engineering, School of Engineering and Digital Sciences, Nazarbayev University, Nur-Sultan 010000, Kazakhstan. [9]Department of Chemical Engineering, Amirkabir University of Technology (Tehran Polytechnic), Tehran, Iran. [10]Department of Polymer Technology, Faculty of Chemistry, Gdańsk University of Technology, G. Narutowicza 11/12, 80-233 Gdańsk, Poland. ✉email: sajjad.habibzadeh@mail.mcgill.ca; amin.hamed.m@gmail.com

silicone-germanium (SiGe)[23], silicone-carbide[24], and beryllium-oxide (Be-O)[25,26] form planar heterostructures to produce nanosheets with tunable electrical, thermal, and mechanical properties[27].

The boron-carbide nanosheets (BC_3NSs), as a carbonaceous semiconductor, possess a bandgap ranging from 0.4 to 0.7 eV. Concerning the theoretical research on physical properties of the BC_3NS, such nanosheets have room temperature Young's modulus, tensile strength, and thermal conductivity of 256, 29.0 N m^{-1}, 410 W m^{-1} K^{-1}, respectively[28]. Moreover, the integration of BC_3NSs with a similar lattice structure with graphene forms in-plane heterostructures composed of BC_3NS and graphene with tunable properties. However, BC_3NS-graphene hetero-nanosheets (BC_3GrHs) may not be ideally acquired as a perfect lattice because of topological defects at the juncture of grain boundaries containing non-hexagonal rings, i.e., heptagons and pentagons. Typically, more difficulties may also be brought about at elevated temperatures, such that the inter-particle distance would be increased because of attenuated molecular motions. Thus, the boundary regions are unavoidably under more stress and may damage. In fact, defects weaken the physical and mechanical properties of BC_3NS under overheating conditions[22].

Due to the potential overheating of the heterostructure nanosheets applied in nano-electronics and storage devices, understanding the thermal transport along such nanodevices is significant to estimate their lifetime and performance. In this regard, several theoretical studies attempted to predict the thermal properties of the heterostructure nanosheets. For example, Li et al.[29] studied the thermal properties of heterostructure nanosheet composed of graphene and hexagonal BN using molecular dynamics (MD) simulation. They modeled several graphene-BN heterostructures having grain boundaries with various defect densities of heptagons and pentagons. It was reported that the interfacial conductance decreased from 5.4×10^{10} to 3.0×10^{10} W m^{-2} K^{-1} upon an increase of mismatch rotation angle of grains from 10° to 25°, and subsequently increasing the density of defects in grain boundaries. Mortazavi et al.[30] verified thermal conductivity in graphene-borophene heterostructure nanosheets using MD simulation and density functional theory (DFT). They reported that the thermal conductance in grain boundaries was not intensively affected by the topology of defects so that the thermal conductance varied in the range of 0.26–36 GW m^{-2} K^{-1}. The effects of vacancy defects in grain boundary and strain on interfacial thermal conductivity of graphene-BN heterostructure nanosheet were shown in the theoretical works done by Son et al.[31]. However, vacancy defects were found as the leading cause of enhanced interfacial thermal conductance; however, with lower inherent thermal conductivity.

Moreover, the increase of the strain caused a decrease in interfacial thermal conductance. Yao et al.[32] reported the effects of vacancy defect, strain, and temperature fields on the interfacial thermal transport of grain boundary in graphene-BN heterostructure by MD simulation, notifying enhanced heat transfer from grain boundaries at higher temperatures. At the same time, an inverse trend was observed once the size of the defect increased. Moreover, the compression strain could not significantly affect the interfacial thermal conductivity. Sadeghzadeh et al.[33], studied the mechanical properties of defective hybrid C_3N-BC_3 nanosheets.

So far, parameters affecting the thermal conductivity and temperature profile of the heterostructure nanosheets, such as defect density in the grain boundary, strain, and temperature, are studied. However, there is no image of thermal properties of BC_3GrHs heterostructure, neither theoretically nor experimentally. Theoretical investigation of such phenomenon would help deepen understanding of the performance of such complex conductive materials needed for future developments in electronics, military, and aerospace applications. In the present work, we demonstrated the temperature profile along BC_3GrHs together with visualization of the interfacial thermal resistance (Kapitza resistance) in the grain boundaries using MD simulations. The temperature profiles of BC_3GrHs with grain boundaries (containing symmetric and asymmetric pentagons and heptagons with various defect concentrations) were first tested at 300 K and $\Delta T = 40$ K. Next, the effects of temperature changes, temperature gradient (ΔT), and strain on Kapitza resistance of BC_3GrHs having grain boundaries were unveiled and discussed.

Simulation method

In this research, MD simulation by open-source software Large-Scale Atomic/Molecular Massively parallel Simulator (LAMMPS)[34] was applied to investigate the thermal properties of BC_3GrHs having grain boundaries containing symmetric and asymmetric pentagon-heptagon defect pairs with various defect concentrations. The bonding interactions of carbon–carbon and carbon-Boron were modeled using the optimized Tersoff potential[35]. Figure 1 shows the flowchart of simulation stages, including the structure and framework of the modeling, along with energy minimization, stress relaxation, and computation of thermal properties.

Figure 2 shows the atomic configuration of the symmetric and asymmetric grain boundaries containing pentagon-heptagon pairs. Notably, perfect grain boundaries in BC_3GrHs consist of hexagons. As in Fig. 2, A1, A2, A3 schematics are related to the symmetric grain boundaries having ring series of pentagon-heptagon-hexagon-hexagon (5–7–6–6), pentagon-heptagon-hexagon (5–7–6), and pentagon-heptagon- pentagon-heptagon (5–7–5–7), respectively. A_4, A_5, and A_6 schematics correspond to the asymmetric grain boundaries having ring series of pentagon-heptagon-hexagon-hexagon (5–7–6–6), pentagon-heptagon-hexagon (5–7–6), and pentagon-heptagon- pentagon-heptagon (5–7–5–7). In other words, 5–7–6–6 configurations (A_1, A_4), 5–7–5–7 configurations (A_3, A_6) have the lowest and highest defect density, respectively, along grain boundaries. Moreover, two, one, and zero hexagonal rings separated two 5–7 defect pairs in A_1 (or A_4), A_2 (or A_5), and A_3 (or A_6) configurations, respectively.

The width and length of all BC_3GrHs were 10 and 30 nm, respectively. The periodic boundary conditions were considered in both X and Y directions.

Figure 3 represents MD setup for computing the temperature gradient along the heat transfer direction and Kapitza resistance in grain boundaries. For these purposes, the nanosheet models were divided into 30 slabs along the X-direction. Atoms present in the left and right edges of nanosheets were fixed. Applying the NVT ensemble
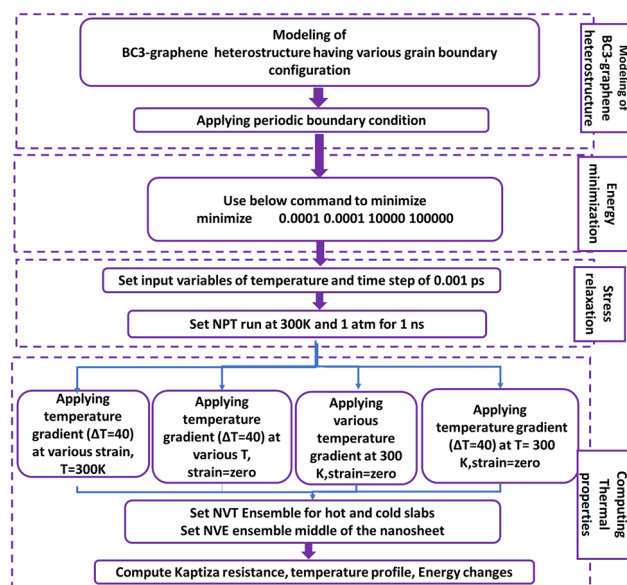
Figure 1. Flowchart of the overall simulation stages, including modeling, energy minimization, stress relaxation and calculation of thermal properties.

(Nose–Hoover thermostat method), the temperature at the hot and cold slabs were defined as $T + \Delta T/2$ and $T - \Delta T/2$, respectively. The heat flux (J_x) along the X direction in nanosheets is expressed as below[36]:

$$J_x = \frac{dE/dt}{A} \tag{1}$$

where A_c is the cross-section area of the nanosheet, t is simulation time, and E is accumulated energy. The thickness of nanosheets was considered 3.62 Å, which was the average value of van der Waals diameters of carbon (3.4 Å) and boron (3.84 Å)[37].

Furthermore, it is possible to establish a relationship between the heat flux (q_x), and the temperature drop in grain boundary (ΔT_{GB}) as following equation in which R_k is the interfacial thermal resistance in grain boundary (Kapitza resistance)[38]:

$$R_k = \frac{\Delta T_{GB}}{J_x} \tag{2}$$

After the calculating Kapitza resistance of grain mentioned above boundaries in BC$_3$GrHs, and obtaining temperature profile along BC$_3$GrHs having various grain boundaries at T = 300 K and ΔT = 40 K, the effect of temperature increase (from 300 to 650 K), changes of temperature gradient (ΔT in range of 20–55 K), and applying strain (from 0.01 to 0.08%) on Kapitza resistance were verified.

Results and discussion

Due to the inevitable presence of the grain boundaries consisting of pentagon-heptagon pairs in the structure of BC$_3$GrHs, which cause the creation of Kapitza resistance and affect the temperature profile and energy changes, in the following sections, we placed the focus on verifying the mentioned thermal properties.

Temperature profile and heat current evaluation in BC$_3$GrHs.

To obtain more insight into the effect of grain boundary on the thermal properties of the BC$_3$GrHs, the changes of temperature along nanosheets were determined. Figure 4a and b show the temperature profiles of the BC$_3$GrHs having various types of grain boundaries (A$_1$, A$_2$, A$_3$, A$_4$, A$_5$, and A$_6$) along X direction at room temperature and temperature gradient of 40 K. The temperature profiles of all nanosheets having grain boundaries containing heptagon-pentagon pairs revealed discontinuity in the middle so that the temperature dropped dramatically in the grain boundary placed at X = 15 nm. It can be speculated that pentagons and heptagons in the grain boundaries act as topological defects, which assist phonon scattering in the middle of BC$_3$GrHs, ending in a temperature drop (ΔT$_{GB}$). Li et al.[29] reported a similar nonlinearity in temperature profile for graphene-boron nitride heterostructure having 5–7 defects along the grain boundaries. In another MD simulation, Mayelifartash et al.[39] reported a temperature drop at the C3N and BC3 nanosheets interface in the hybrid C$_3$N-BC$_3$ nanosheets.

Figure 4 also suggests an increase in temperature drop upon increasing the defect density in grain boundaries, which means that the BC$_3$GrHs with 5–7 and 5–7–5–7 defect pairs show the lowest and highest temperature drop, respectively. This can be ascribed to enhanced phonon scattering in grain boundaries having higher defect concentration. Moreover, the temperature drop in non-symmetric grain boundaries was higher than that of
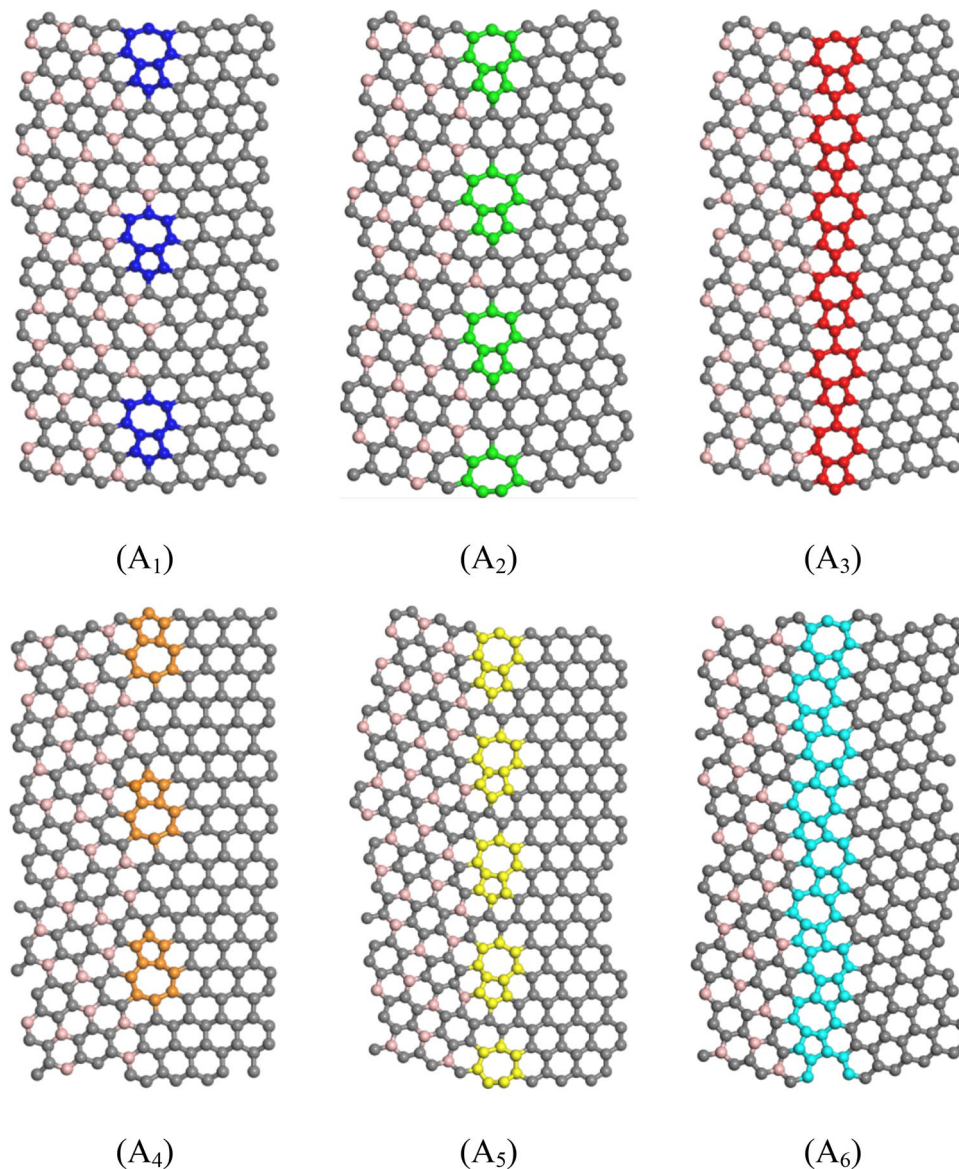
Figure 2. Top views of the atomic configuration of six different grain boundaries consisting of pentagon-heptagon defect pairs with different defect concentrations: (A$_1$) 5–7–6–6–s, (A$_2$) 5–7–6–s, (A$_3$) 5–7–5–7–s, (A$_4$) 5–7–6–6–a, (A$_5$) 5–7–6–a, and (A$_6$) 5–7–5–7–a. "s" and "a" denote as symmetric and asymmetric, respectively.
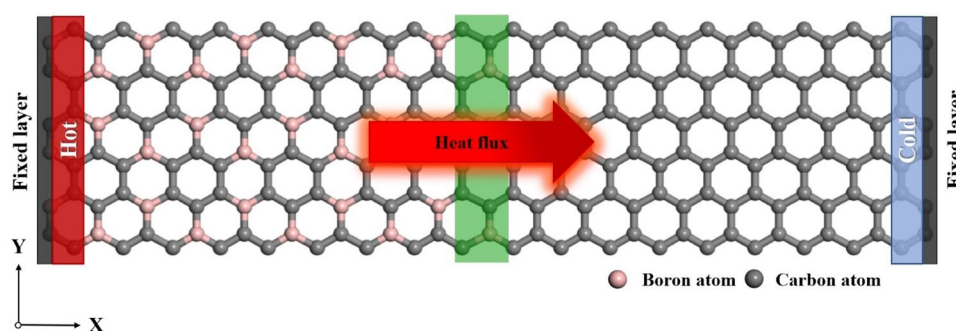

Figure 3. MD setup for evaluating thermal properties of BC$_3$GrHs. Gray and pink balls denote carbon and boron atoms, respectively. The periodic boundary condition is applied along the X and Y directions. The heat flux is in the X-direction. The green, red, and blue regions show the grain boundary, hot slab, and cold slab, respectively. The visualization was ob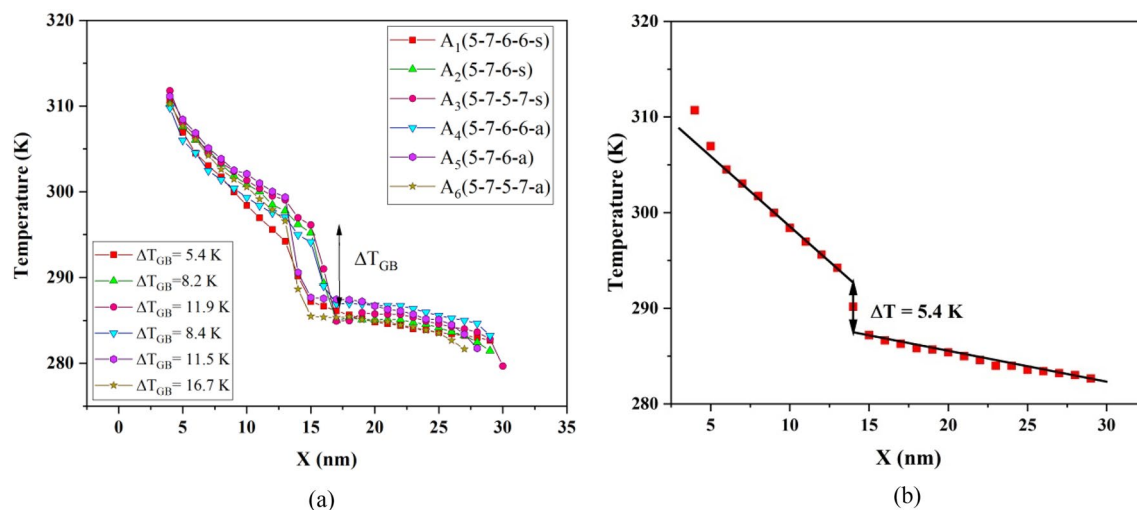tained by means of visual MD (VMD) simulation (Ver. 1.9.3, https://www.ks.uiuc.edu/Development/Download/download.cgi?PackageName=VMD).

Figure 4. (**a**)The steady-state one-dimension temperature profiles for BC_3GrHs having grain boundaries-type A_1, A_2, A_3, A_4, A_5, A_6 along X direction with the same length of 30 nm at T = 300 K and ΔT = 40 K. ΔT_{GB} is the temperature drop in the grain boundary, (**b**) the linear fitting performed on the temperature profile for BC_3GrHs having grain boundary-type A_1 to obtain temperature drop (ΔT) at the grain boundary.
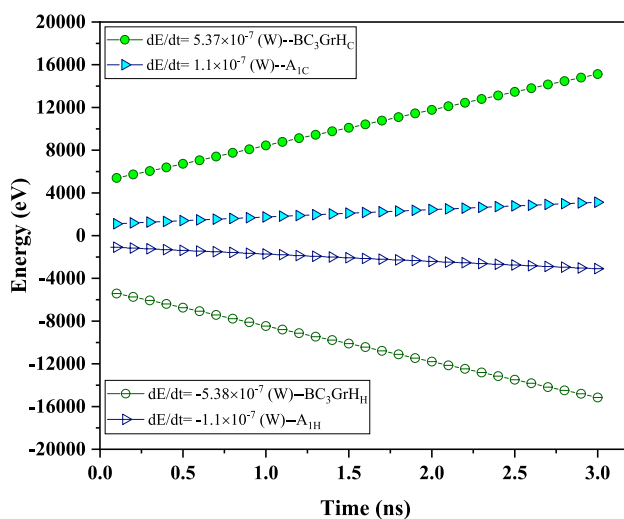

Figure 5. Change in the amounts of energy in the cold (C-coded symbols) and hot (H-coded symbols) slabs as a function of simulation time for BC_3GrH having perfect grain boundary (hexagonal rings) and BC_3GrH having grain boundary-type A_1 (5–7–6–6–s), with the same lengths and width of 30 nm and 10 nm, respectively, at T = 300 K and ΔT = 40 K. Filled symbols indicate effluent of H slab, while hollow symbols indicate heat entered into the C slab.

symmetric grain boundaries at the specified defect concentration. A similar trend for temperature drop in the vicinity of grain boundaries, having mentioned pentagon-heptagon defect pairs, was reported for polycrystalline silicene by Khalkhali et al.[40].

Figure 5 compares the simulation outputs in terms of time-dependent energy of the hot and cold slabs in BC_3GrH structure with grain boundaries of A_1 (5–7–6–6–s) type, besides, BC_3GrH with perfect grain boundary of hexagonal rings type at fixed T = 300 K and ΔT = 40 K. The figure also makes it possible to compare heat flux values $\left(\frac{dE}{dt}\right)$ of hot and cold slabs. Expectedly, a descending and an ascending linear trend in energy variation over simulation time are the cases for the hot and cold slabs of nanosheets, respectively. Furthermore, we can see that the absolute amounts of energy in the cold and hot zones are approximately equal, which means conservation of energy or model verification. The same trend of energy variation in the hot and cold slabs was observed in the polycrystalline BC3 nanosheets, which confirms that the total energy of each simulated system remained constant[41]. In another theoretical research performed by Yousefi et al.[42], the calculation of the accumulated energy in the hot and cold slabs of nanoporous graphene revealed a similar trend.
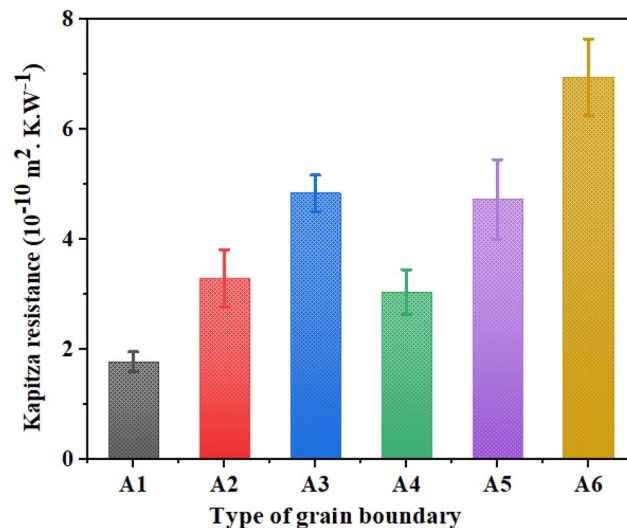
Figure 6. The interfacial thermal resistance (Kapitza resistance) of various constructed grain boundaries A_1 (5–7–6–6–s), A_2 (5–7–6–s), A_3 (5–7–5–7–s), A_4 (5–7–6–6–a), A_5 (5–7–6–a), and A_6 (5–7–5–7–a) in BC$_3$GrHs at T = 300 K and ΔT = 40 K. "s" and "a" denote as symmetric and asymmetric.

The comparison between the rates of heat transfer or heat flux values, featured by the considerable difference between the slopes of energy variation plots (Fig. 5), makes evident that BC$_3$GrH with a perfect grain boundary characteristic is more sensitive to the time compared to the corresponding structure with grain boundaries of type A_1. A considerably higher rate of heat transfer in defect-free BC$_3$GrH nanosheet is indicative of a significantly lower resistance against phonon transfer because of architecturally ordered hexagonal grain boundaries allowing diffusion of phonons. On the other hand, the non-uniform grain boundaries in A_1 (5–7–6–6–s) polygonal BC$_3$GrH nanosheet cause an additional resistance resulting from the collision between highly scattered phonons. Since the interface region at BC$_3$-GrH juncture dissipates energy, and the phonon spectrum of atoms in both sides of the grain boundaries dissipates the energy, such a drop in the heat flux of non-uniform structures would be speculated[43].

Kapitza resistance of grain boundaries containing pentagons and heptagons in BC$_3$GrHs. After calculating the values of the heat current and temperature drop at grain boundaries, the interfacial thermal resistance (Kapitza resistance) values at six mentioned grain boundaries were compared. Figure 6 demonstrates the values of Kapitza resistance of grain boundaries A_1 (5–7–6–6–s), A_2(5–7–6–s), (A_3) 5–7–5–7–s, A_4 (5–7–6–6–a), A_5 (5–7–6–a), and A_6 (5–7–5–7–a) in BC$_3$GrHs at T = 300 K and ΔT = 40 K. As can be observed, Kapitza resistance increased by increasing the defect concentration in grain boundaries so that A_1 and A_3 showed the lowest (2×10^{-10} m^2 K W^{-1}) and highest (4.9×10^{-10} m^2 K W^{-1}) values, respectively, among symmetric grain boundaries. For non-symmetric grain boundaries, the values of Kapitza resistance varied in the range of $3.1–7.2 \times 10^{-10}$ m^2 K W^{-1}. As mentioned before, the grain boundary having a higher defect density caused more diverse lattice structures along the heat current direction between two grains. This caused the higher phonon scattering rate in the grain boundary, which acted as a barrier front heat flow and increased Kapitza thermal resistance.

Moreover, the non-symmetric grain boundaries showed higher Kapitza resistance than the symmetric one at specified defect concentration due to the higher phonon–phonon scattering. The observed increasing trend for Kapitza resistance by increasing defect density is in good agreement with the obtained results for MoS$_2$ single-layer heterostructures reported by Mortazavi et al.[44]. In another work performed by Yao et al.[32], the interfacial thermal conductivity of grain boundary in graphene-BN planar heterostructure decreased by increasing the percentage of vacancy defects at the interface. Likewise, Lio et al.[45] showed the effect of defect density of grain boundary presented in bicrystal ZnO on the Kapitza thermal resistance, which revealed the same trend.

Effect of temperature on Kapitza resistance. To evaluate the effect of elevated temperature on Kapitza resistance of grain boundaries, the values of Kapitza resistance of grain boundaries-type A_1, A_2, A_3, A_4, A_5, and A_6 at various temperatures of 350 K, 400 K, 450 K, 500 K, 550 K, 600 K, 650 K were computed. Figure 7 shows the alteration in Kapitza resistance of grain boundaries as a function of temperature at $\Delta T = 40$ K and zero strain. As seen, the Kapitza resistance of all types of grain boundaries decreased by elevating temperature. For example, for A_6 and A_3, the Kapitza resistance decreased from the values of 7.2×10^{-10} and 4.9×10^{-10} m^2 K W^{-1} to the values of 4.3×10^{-10} and 1.5×10^{-10} m^2 K W^{-1} with decrement of about 40% and 69.3%, respectively by increasing the temperature from 300 to 650 K. It can be explained that the temperature enhancement caused the excitement of high-frequency phonons and subsequently simplification of phonon transmission. Therefore, the presence of phonons possessing higher energy facilitated the heat flux along the grain boundary and resulted in higher interfacial thermal conductivity and lower Kapitza resistance[46]. A similar effect of the temperature elevation on
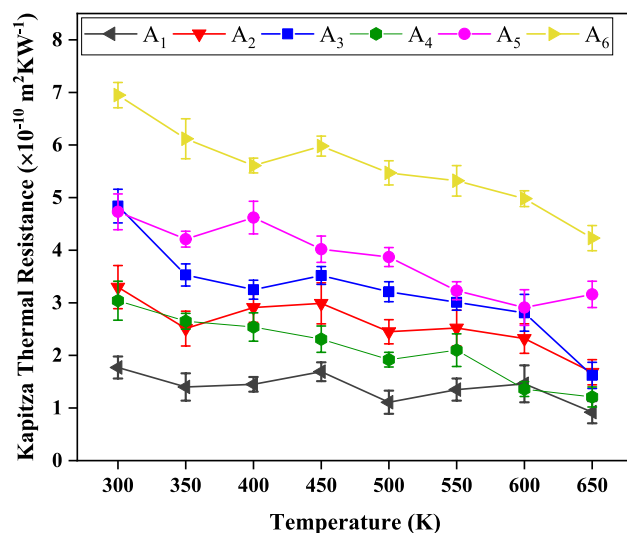
Figure 7. The changes in Kapitza thermal resistance of six constructed grain boundaries A_1 (5–7–6–6–s), A_2(5–7–6–s), A_3 (5–7–5–7–s), A_4 (5–7–6–6–a), A_5 (5–7–6–a), and A_6 (5–7–5–7–a) in BC_3GrHs as a function of temperature at $\Delta T = 40$ K and zero strain.
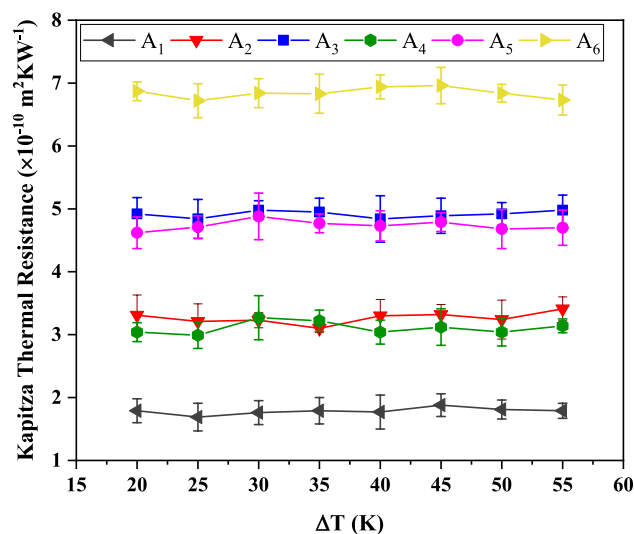

Figure 8. The changes in Kapitza thermal resistance of six constructed grain boundaries A_1 (5-7-6–6-s), A_2 (5-7-6-s), A_3 (5–7–5–7–s), A_4 (5–7–6–6–a), A_5 (5–7–6–a), and A_6 (5–7–5–7–a) in BC_3GrHs as a function of ΔT at 300 K and zero strain.

Kaptiza resistance was observed for graphene-boron nitride hetero-nanosheets in the works done by Eshkalak et al.[47] and Liu et al.[48].

Effect of temperature gradient (ΔT) on Kapitza resistance. The temperature gradient is considered as a determining parameter on heat current in BC_3GrHs. However, to clarify its effect on Kapitza resistance of the grain boundaries, in this section, the variation in Kapitza resistance at various temperature gradients (ΔT) is verified. The changes in Kapitza thermal resistance of grain boundaries-type A_1, A_2, A_3, A_4, A_5, and A_6 in BC_3GrHs as a function of ΔT at 300 K and zero strain are depicted in Fig. 8. As seen, the values of Kapitza resistance of all grain boundaries vary in a narrow range, which confirms that the Kapitza resistance is independent of ΔT variation.

According to the definition of the Kapitza resistance $\left(R_k = \frac{\Delta T_{GB}}{\frac{dE/dt}{A}} \right)$, the change in ΔT caused the variation in both ΔT_{GB} and dE/dt equally, which at least resulted in minor changes in the value of Kapitza resistance.
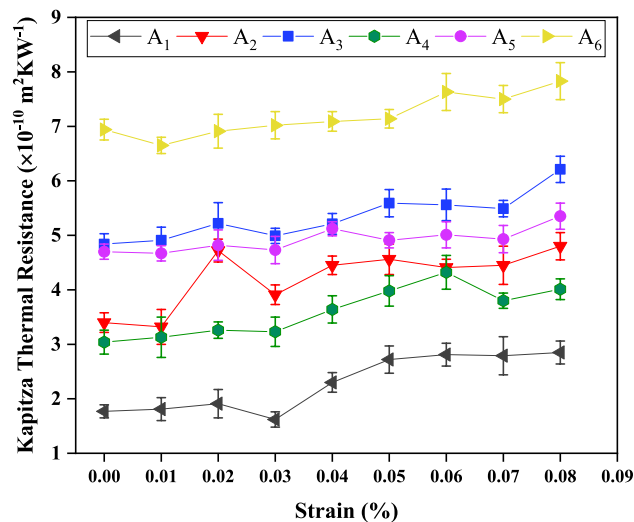
Figure 9. The changes in Kapitza thermal resistance of six constructed grain boundaries A_1 (5–7-6–6-s), A_2 (5–7-6-s), A_3 (5–7–5–7–s), A_4 (5–7–6–6–a), A_5 (5–7–6–a), and A_6 (5–7–5–7–a) in BC$_3$GrHs as a function of strain at $\Delta T = 40$ K and $T = 300$ K.
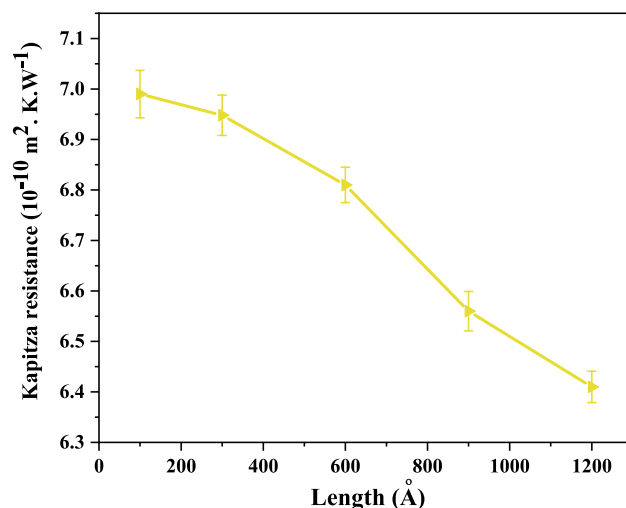

Figure 10. The changes in Kapitza thermal resistance of constructed grain boundaries A_6 (5–7–5–7–a) in BC$_3$GrHs function of nanosheet length at $\Delta T = 40$ K and $T = 300$ K.

Effect of strain on Kapitza resistance. Due to the possible creation of mechanical strain in BC$_3$GrHs, whether synthetic or intrinsically, it is important to understand the strain-thermal properties relationship. Figure 9 shows the alteration in Kapitza resistance of grain boundaries-type A_1 to A_6 as a function of strain at room temperature and $\Delta T = 40$ K. It can be observed that the rise of the strain caused the increase in Kapitza resistance of all grain boundaries. For instance, the Kapitza resistance of grain boundaries type-A_3 and A_6 increased from the values of 4.9×10^{-10} and 6.94×10^{-10} m^2 K W^{-1} to the values of 6.3×10^{-10} and 7.9×10^{-10} m^2 K W^{-1} with an increment of about 22.22% and 13.8%, respectively. The increase of strain in the direction of heat current caused the increment of bond length and subsequently weakened atomic interaction.

Moreover, the phonon speed of atoms decreased by increasing the strain. These two outcomes arising from strain increment led to the decrease in Kapitza resistance. Eshkalak et al.[46] reported a similar effect of strain on Kapitza resistance of grain boundary in C$_3$N-graphene heterostructure.

Effect of Length on Kapitza resistance. Another parameter that may affect the Kaptiza resistance is the length of the nanosheet as a scale of the length of the heat transfer path. Figure 10 shows the alteration of Kapitza thermal resistance of the constructed grain boundaries A_6 (5–7–5–7–a) in the BC$_3$GrHs as a function of the length of the nanosheet. The Kapitza thermal resistance in grain boundary decreased from the value of 6.99×10^{-10} m^2 K W^{-1} to the value of 6.4×10^{-10} m^2 K W^{-1} by increasing the length of the nanosheet from 100 to 1200 Å. A similar

decreasing trend in Kapitza resistance of grain was observed in Azizi *et al.*[49] by increasing the nanosheet length. In another MD simulation performed by Jones *et al.*[50], the Kapitza thermal resistance in aluminum/Gallium nitride bicrystal decreased by increasing the length. It can be explained that the predicted thermal conductivity by MD simulation depends on the system length along the heat flux direction, as the below equation predicts[42]:

$$\frac{1}{K_L} = \frac{1}{K_\infty}\left(1 + \frac{\lambda}{L}\right) \tag{3}$$

where K_∞, L, and λ refer to the thermal conductivity of the finite sample, the length of the nanosheet, and the phonon mean free path, respectively. As can be seen, the thermal conductivity increased against the length of the sample. The formula can be rewritten to. $K_L = K_\infty\left(\frac{L}{L+\lambda}\right)$ and subsequently placed in the equation of $J_x = K_L\frac{\Delta T}{L}$ so that the equation of $J_x = K_\infty\left(\frac{\Delta T}{L+\lambda}\right)$ would be obtained. The multiplication of K_∞ and ΔT is a constant value. By substituting the J_x in the $R_k = \frac{\Delta T_{GB}}{J_x}$, the relation between R_k and the length of the sample is obtained as $R_k = \frac{\Delta T_{GB}(L+\lambda)}{K_\infty \times \Delta T}$. However, it is known that the ΔT_{GB} also changes with the changes of the length $\left(\Delta T_{GB}\alpha L^\beta\right)$. Therefore, according to the decreasing trend in the R_k by an increase of the length, it is obvious that β has a value smaller than -1.

Conclusion

In the current work, the thermal properties of BC$_3$NS-graphene hetero-nanosheets (BC$_3$GrHs) having various types of grain boundaries [A$_1$ (5–7–6–6–s), A$_2$ (5–7–6–s), A$_3$ (5–7–5–7–s), A$_4$ (5–7–6–6–a), A$_5$ (5–7–6–a), and A$_6$ (5–7–5–7–a)] were studied through MD simulation. First, the temperature profile along BC$_3$GrHs was plotted to verify the temperature drop in grain boundary (ΔT_{GB}) at T = 300 K, ΔT = 40 K, and zero strain. It was observed that all temperature profiles showed discontinuity in the middle and ΔT_{GB} increased by increasing the defect density in grain boundaries so that the BC$_3$GrHs having 5–7 and 5–7–5–7 defect pairs had the lower and higher ΔT_{GB}, respectively. This happened due to the more phonon scattering in grain boundaries having higher defect concentration. Moreover, the temperature drop in asymmetric grain boundaries was higher than that of symmetric grain boundaries at the specified defect concentration. Next, the Kapitza resistance of mentioned grain boundaries and several parameters such as temperature and temperature gradient (ΔT) on its variation was investigated. It was revealed that Kapitza resistance increased by increasing the defect concentration in grain boundaries due to the higher phonon scattering rate in the grain boundary, which acted as a barrier in front of the heat flow and caused the increase in Kapitza thermal resistance. For example, A$_1$ and A$_3$ had the lowest (2×10^{-10} m^2 K W^{-1}) and highest (4.9×10^{-10} m^2 K W^{-1}) values of Kapitza resistance, respectively, among symmetric grain boundaries.

Moreover, the non-symmetric grain boundaries showed higher Kapitza resistance than the symmetric one at specified defect concentration. The temperature elevation caused the decrease of the Kapitza resistance due to increasing the energy of phonons which facilitated the heat flux along grain boundaries. The changes of the ΔT could not considerably affect the alteration of Kapitza resistance. The increase of strain caused the enhancement of Kapitza resistance due to a decrease in the phonon speed of atoms. The methodology implemented in the present work can be generalized to more complex nanostructures to predict and precisely adjust thermal properties of other heterostructures.

References

1. Young, R. J. *et al.* The mechanics of graphene nanocomposites: a review. *Compos. Sci. Technol.* **72**(12), 1459–1476 (2012).
2. Srinivas, G. *et al.* Synthesis of graphene-like nanosheets and their hydrogen adsorption capacity. *Carbon* **48**(3), 630–635 (2010).
3. Balandin, A. A. *et al.* Superior thermal conductivity of single-layer graphene. *Nano Lett.* **8**(3), 902–907 (2008).
4. Farzadian, O., Spitas, C. & Kostas, K. V. Graphene-carbon nitride interface-geometry effects on thermal rectification: a molecular dynamics simulation. *Nanotechnology* **32**(21), 215403 (2021).
5. Farzadian, O. *et al.* Phonon thermal rectification in hybrid graphene-C3N: a molecular dynamics simulation. *Nanotechnology* **31**(48), 485401 (2020).
6. Wu, Z.-S. *et al.* Synthesis of graphene sheets with high electrical conductivity and good thermal stability by hydrogen arc discharge exfoliation. *ACS Nano* **3**(2), 411–417 (2009).
7. Stoller, M. D. *et al.* Graphene-based ultracapacitors. *Nano Lett.* **8**(10), 3498–3502 (2008).
8. Revuri, V. & Lee, Y.-K. 2D Material-based hybrid nanostructure for diagnosis and therapy. In *Biomedical Applications of Graphene and 2D Nanomaterials* 143–164 (Elsevier, 2019).
9. Nalwa, H. S. *Handbook of Nanostructured Materials and Nanotechnology, Five-Volume Set* (Academic Press, 1999).
10. Farajpour, A., Ghayesh, M. H. & Farokhi, H. A review on the mechanics of nanostructures. *Int. J. Eng. Sci.* **133**, 231–263 (2018).
11. Zarghami Dehaghani, M. *et al.* Shape memory thin films of Polyurethane: Does graphene content affect the recovery behavior of Polyurethane nanocomposites?. *Polym. Compos.* **41**(8), 3376–3388 (2020).
12. Novoselov, K. S. *et al.* Electric field effect in atomically thin carbon films. *Science* **306**(5696), 666–669 (2004).
13. Li, X. *et al.* Graphene in photocatalysis: a review. *Small* **12**(48), 6640–6696 (2016).
14. Lei, W. *et al.* Porous boron nitride nanosheets for effective water cleaning. *Nat. Commun.* **4**(1), 1–7 (2013).
15. Hamed, M. A., Fereidoon, A. & Ahangari, M. G. Atomistic modeling of interfacial interaction between polyvinyl chloride and polypropylene with Boron-Nitride monolayer sheet: a density functional theory study. *Superlattices Microstruct.* **111**, 23–31 (2017).
16. Zarghami, D.M., *et al.* Insight into the self-insertion of a protein inside the boron nitride nanotube. *ACS Omega* (2020).
17. Bagheri, B. *et al.* Correlation between surface topological defects and fracture mechanism of γ-graphyne-like boron nitride nanosheets. *Comput. Mater. Sci.* **5**, 110152 (2020).

18. Dehaghani, M. Z. *et al.* Boron nitride nanotube as an antimicrobial peptide carrier: a theoretical insight. *Int. J. Nanomed.* **16**, 1837 (2021).
19. Dehaghani, M. Z. *et al.* Insight into the self-insertion of a protein inside the boron nitride nanotube. *ACS Omega* **5**(49), 32051 (2020).
20. Salmankhani, A. *et al.* A theoretical scenario for the mechanical failure of boron carbide nanotubes. *Comput. Mater. Sci.* **186**, 110022 (2021).
21. Dadrasi, A. *et al.* A theoretical insight into the fracture behavior of the edge-cracked polycrystalline BC3 nanosheets. *Comput. Mater. Sci.* **192**, 110345 (2021).
22. Bagheri, B. *et al.* Fracture fingerprint of polycrystalline C3N nanosheets: theoretical basis. *J. Mol. Gr. Modell.* **120**, 107899 (2021).
23. Dehaghani, M. Z. *et al.* Fracture mechanics of SiGe-nano-sheets using molecular dynamics study: mechanics of monocrystalline versus polycrystalline structure. *Eng. Fracture Mech.* **20**, 107782 (2021).
24. Molaei, F. *et al.* Applying molecular dynamics simulation to take the fracture fingerprint of polycrystalline SiC nanosheets. *Comput. Mater. Sci.* **200**, 110770 (2021).
25. Dehaghani, M. Z. *et al.* Fracture toughness and crack propagation behavior of nanoscale beryllium oxide graphene-like structures: a molecular dynamics simulation analysis. *Eng. Fracture Mech.* **235**, 107194 (2020).
26. Dehaghani, M. Z. *et al.* Fracture mechanics of polycrystalline beryllium oxide nanosheets: a theoretical basis. *Eng. Fracture Mech.* **244**, 107552 (2021).
27. Grüneis, A. & Vyalikh, D. V. Tunable hybridization between electronic states of graphene and a metal surface. *Phys. Rev. B* **77**(19), 193401 (2008).
28. Mortazavi, B. *et al.* Outstanding strength, optical characteristics and thermal conductivity of graphene-like BC3 and BC6N semi-conductors. *Carbon* **149**, 733–742 (2019).
29. Li, Y. *et al.* Mechanical and thermal properties of grain boundary in a planar heterostructure of graphene and hexagonal boron nitride. *Nanoscale* **10**(7), 3497–3508 (2018).
30. Mortazavi, B. *et al.* Machine-learning interatomic potentials enable first-principles multiscale modeling of lattice thermal conductivity in graphene/borophene heterostructures. *Mater. Horiz.* **7**(9), 2359–2367 (2020).
31. Song, J. *et al.* Effect of strain and defects on the thermal conductance of the graphene/hexagonal boron nitride interface. *Phys. Chem. Chem. Phys.* **22**(20), 11537–11545 (2020).
32. Yao, W. & Fan, L. Defects in graphene/h-BN planar heterostructures: insights into the interfacial thermal transport properties. *Nanomaterials* **11**(2), 500 (2021).
33. Mayelifartash, A., Abdol, M. A. & Sadeghzadeh, S. Mechanical properties of intrinsic and defective hybrid polyaniline (C 3 N)-BC 3 nanosheets in the armchair and zigzag configurations: a molecular dynamics study. *Appl. Phys. A* **126**(11), 1–16 (2020).
34. Plimpton, S. Fast Parallel Algorithms for Short-Range Molecular Dynamics. *J. Comput. Phys.* **117**(1), 1–19 (1995).
35. Kınacı, A. *et al.* Thermal conductivity of BN-C nanostructures. *Phys. Rev. B* **86**(11), 115410 (2012).
36. Khadem, M. H. & Wemhoff, A. P. Comparison of Green-Kubo and NEMD heat flux formulations for thermal conductivity prediction using the Tersoff potential. *Comput. Mater. Sci.* **69**, 428–434 (2013).
37. Mantina, M. *et al.* Consistent van der Waals Radii for the whole main group. *J. Phys. Chem. A* **113**(19), 5806–5812 (2009).
38. Rajabpour, A. & Volz, S. Universal interfacial thermal resistance at high frequencies. *Phys. Rev. B* **90**(19), 195444 (2014).
39. Mayelifartash, A., Abdol, M. A. & Sadeghzadeh, S. Thermal conductivity and interfacial thermal resistance behavior for the poly-aniline (C3N)–boron carbide (BC3) heterostructure. *Phys. Chem. Chem. Phys.* **20**, 10239 (2021).
40. Khalkhali, M., Rajabpour, A. & Khoeini, F. Thermal transport across grain boundaries in polycrystalline silicene: a multiscale modeling. *Sci. Rep.* **9**(1), 1–12 (2019).
41. Fooladpanjeh, S. *et al.* Thermal conductivity of random polycrystalline BC3 nanosheets: A step towards realistic simulation of 2D structures. *J. Mol. Gr. Modell.* **107**, 107977 (2021).
42. Yousefi, F., Khoeini, F. & Rajabpour, A. Thermal conductivity and thermal rectification of nanoporous graphene: a molecular dynamics simulation. *Int. J. Heat Mass Transf.* **146**, 118884 (2020).
43. Mortazavi, B. *et al.* Strong thermal transport along polycrystalline transition metal dichalcogenides revealed by multiscale modeling for MoS2. *Appl. Mater. Today* **7**, 67–76 (2017).
44. Mortazavi, B. & Rabczuk, T. Multiscale modelling of heat conduction in all-MoS 2 single-layer heterostructures. *RSC Adv.* **7**(18), 11135–11141 (2017).
45. Liu, Y. *et al.* Effect of grain boundary angle on the thermal conductivity of nanostructured bicrystal ZnO based on the molecular dynamics simulation method. *Int. J. Heat Mass Transf.* **145**, 118791 (2019).
46. Einalipour Eshkalak, K., Sadeghzadeh, S. & Molaei, F. Interfacial thermal resistance mechanism for the polyaniline (C3N)–graphene heterostructure. *J. Phys. Chem. C* **124**(26), 14316–14326 (2020).
47. Eshkalak, K. E., Sadeghzadeh, S. & Jalaly, M. Thermal resistance analysis of hybrid graphene-boron nitride nanosheets: the effect of geometry, temperature, size, strain and structural defects. *Comput. Mater. Sci.* **174**, 109484 (2020).
48. Liu, F. *et al.* Enhancement of thermal energy transport across the graphene/h-BN heterostructure interface. *Nanoscale* **11**(9), 4067–4072 (2019).
49. Azizi, K. *et al.* Kapitza thermal resistance across individual grain boundaries in graphene. *Carbon* **125**, 384–390 (2017).
50. Jones, R. E. *et al.* Investigation of size and electronic effects on Kapitza conductance with non-equilibrium molecular dynamics. *Appl. Phys. Lett.* **102**(18), 183119 (2013).

Acknowledgements

Author contributions

M.Z.D. performed the simulation and wrote the first draft. F.Y. and A.H.M. developed the theoretical formalism and analyzed the data. S.M.S. and A.E. drafted the manuscript. A.M and O.F. checked data collection. A.H.M. and S.H. supervised the study M.R.S. coordinated the study. C.S. analyzed the methodology and critically revised the manuscript. All authors read, commented on the manuscript, gave the final approval for publication, and agreed to be held accountable for the work performed herein.

Competing interests

The authors declare no competing interests.

Additional information

Correspondence and requests for materials should be addressed to S.H. or A.H.M.